frontiers | Frontiers in Energy Research

TYPE Original Research
PUBLISHED 08 August 2022
DOI 10.3389/fenrg.2022.924515

OPEN ACCESS

EDITED BY
Takaya Kubo,
The University of Tokyo, Japan

REVIEWED BY
Masashi Ikegami,
Toin University of Yokohama, Japan
Takeru Bessho,
The University of Tokyo, Japan

*CORRESPONDENCE
Yinglin Wang,
wangyl100@nenu.edu.cn
Xintong Zhang,
xtzhang@nenu.edu.cn

SPECIALTY SECTION
This article was submitted to Solar Energy,
a section of the journal
Frontiers in Energy Research

RECEIVED 20 April 2022
ACCEPTED 06 July 2022
PUBLISHED 08 August 2022

CITATION
Li Y, Wang Y, Lin J, Shi Y, Zhu K, Xing Y, Li X, Jia Y and Zhang X (2022), Solution-plasma-induced oxygen vacancy enhances MoO_x/Pt electrocatalytic counter electrode for bifacial dye-sensitized solar cells.
Front. Energy Res. 10:924515.
doi: 10.3389/fenrg.2022.924515

Solution-plasma-induced oxygen vacancy enhances MoO_x/Pt electrocatalytic counter electrode for bifacial dye-sensitized solar cells

Yanan Li, Yinglin Wang*, Jianfei Lin, Yuming Shi, Kuangyu Zhu, Yanmei Xing, Xiaofei Li, Yuwen Jia and Xintong Zhang*

Center for Advanced Optoelectronic Functional Materials Research, and Key Lab of UV-Emitting Materials and Technology of Ministry of Education, Northeast Normal University, Changchun, China

Bifacial dye-sensitized solar cells (DSCs), harvesting light from both front and rear sides, are potential high-efficiency photovoltaic devices with broad application environments. The electrocatalytic counter electrodes (CEs) of bifacial DSCs could determine the light-harvesting from the rear side and the charge collection of solar cells through electrocatalytic processes. As a result, high-activity and high-transparency CEs are essential for bifacial DSCs. Recently, novel CEs based on strong metal-support interaction (SMSI) have been proven to improve the catalysis and stability of the metal catalytic sites and induce great efficiency increase of bifacial DSCs. However, the contradiction between the transparency and conductivity of support is still a major challenge for the application of SMSI-based CEs on bifacial DSCs. Herein, we utilized a solution plasma (SP) method to introduce oxygen vacancies into a transparent MoO_x support film. These SP-induced oxygen vacancies improved the conductivity of MoO_x and the interaction between the metal Pt catalytic sites and support, thereby enhancing the catalytic activity and transparency of MoO_x/Pt CEs. Consequently, the bifacial DSCs with MoO_x/Pt CEs yielded a high efficiency of 7.56% and 6.41% with the front- and rear-side illumination, respectively. This impressive front-to-rear efficiency ratio of 85% indicates that the SP method has a positive effect in constructing high-performance CEs and other electrocatalytic materials based on the SMSI.

KEYWORDS

dye-sensitized solar cells, electrocatalytic activity, counter electrode, oxygen vacancy, solution plasma process

Introduction

Dye-sensitized solar cells (DSCs) have attracted much attention due to their advantages of simple fabrication, low cost, and multicolor appearances (Chen et al., 2020). Especially, bifacial DSCs can absorb photons from the front and rear sides of the devices, probably leading to an efficiency boost of around ~35%, compared with conventional DSCs only absorbing photons from the front (Ito et al., 2008; Duan et al., 2014; Tian et al., 2020). Furthermore, they have potential prospects in applications such as indoor and building photovoltaics owing to their installation flexibility. In bifacial DSCs, electrocatalytic counter electrodes (CEs) are the important components to determine the device efficiency because they not only facilitate the reduction reaction of the electrolyte through the electrocatalytic process but also control the light harvest of bifacial DSCs from the rear side (Xu et al., 2020). Consequently, numerous works were explored for the high-activity and high-transparency CEs.

Strong metal-support interaction (SMSI) is a powerful strategy to produce high-performance catalytic materials (Tauster and Fung, 1978; Ge et al., 2021). It boosts the activity of catalytic sites due to electron transfer between the metal and supports and prevents the nanosized metal catalytic sites from sintering. Nowadays, SMSI has generated numerous catalytic materials, including Pt-, Pd-, Au-, Cu-, and Ru-based catalysts (Guo et al., 2018; Yu et al., 2019; Zhang et al., 2019; Han et al., 2020; Wang et al., 2021; Yu et al., 2021). Recently, a novel Pt-Mo_2C CE based on SMSI was reported by our group (Wu et al., 2020). It possesses highly dispersed Pt nanoclusters on Mo_2C support and successfully achieved a rear-to-front efficiency of ~75% in bifacial DSCs. However, Mo_2C as a support suffered from poor transmittance in the visible range, hindering the further performance improvement of CEs based on the SMSI strategy.

We notice that transition metal oxides (TMOs) are attractive support for SMSI-based catalysis because the electronic structure of their transition-metal cations facilitates electron transfer between the catalytic sites and TMO support (Tauster, 1987). In addition, their excellent transmittance in the visible range efficiently overcomes the shortage of Mo_2C support, whereas it is a challenge that the insufficient conductivity of TMO support may affect the electrocatalytic activity of CEs. Thus, improving the electrical conductivity of TMO becomes essential for developing high-activity and high-transparency TMO-based SMSI CEs. Oxygen vacancies serve as shallow donors in TMO, increasing the carrier concentration, so introducing oxygen vacancies becomes an effective means to improve the conductivity of TMO (Wang et al., 2012). As a result, oxygen vacancies have been introduced into TMO for conductivity improvement through several methods, including liquid exfoliation, plasma etching, chemical reduction, and thermal treatment (Zheng et al., 2017; Yan et al., 2018; Tran et al., 2019; Li et al., 2020; Wang et al., 2020).

Herein, we utilized the solution plasma (SP) method to introduce oxygen vacancies into the MoO_x support and further prepared SMIS-based MoO_x/Pt CEs for bifacial DSCs. To our best knowledge, this is the first time that the SP method has been presented to design high-performance electrocatalyst electrodes. The SP method could generate numerous highly reactive species including H^+, OH^-, and O^{2-} species to induce oxygen vacancies in TMO in a simple, eco-friendly, and non-reducing-reagent way (Takai, 2014; Jedsukontorn et al., 2018; Pitchaimuthu et al., 2018). MoO_x is used as the support because of the ability to easily introduce oxygen vacancies and its great stability compared with Mo_2C. The SP-induced oxygen vacancies boosted the conductivity of MoO_x films and enhanced the electron transfer between the MoO_x support and Pt catalytic sites. These factors endow MoO_x/Pt CEs obtained by the SP method (named MoO_x/Pt-SP) with higher electrocatalytic activity than the untreated reference sample. In addition, MoO_x/Pt-SP possesses outstanding transparency, which generated only 3.4% of light loss at 550 nm compared with the conductive substrate fluorine-doped tin oxide (FTO). Consequently, the obtained bifacial DSCs with MoO_x/Pt-SP CEs produced a power conversion efficiency (PCE) of 7.56% under the front illumination, which is similar to that of 7.65% for DSCs with the generally used Pt electrode.

Experiment

Preparation of electrocatalytic electrodes

The MoO_x thin films were deposited on a well-cleaned FTO substrate by radio frequency magnetron sputtering. All of the samples were deposited for 2 min in an inert atmosphere of argon with a sputtering pressure of 0.8 Pa after being pre-sputtered for 15 min to remove impurities from the target surface. We then subjected the MoO_x support to SP treatment in deionized water with a discharge time of 1 min and a voltage of 1.5 kV. The next step is that the treated MoO_x support was impregnated in 10 mM/L chloroplatinic acid isopropanol solvent for 1 h at room temperature and then removed and blown dry. Finally, the samples were placed in an annealing furnace and annealed at 450°C for 15 min.

Fabrication of dye-sensitized solar cells

The cleaned FTO was immersed in a $TiCl_4$ aqueous solution (0.04 mol/L) and heated in an oven at 70°C for 30 min. TiO_2 paste with a particle size of 30 nm was scraped by the screen-printing method to obtain a film with a thickness of 12–14 μm and then annealed at 500°C for 30 min in a muffle furnace. After the samples were post-treated with a $TiCl_4$ aqueous solution for 20 min and sintered at 500°C, the TiO_2 photoanode was

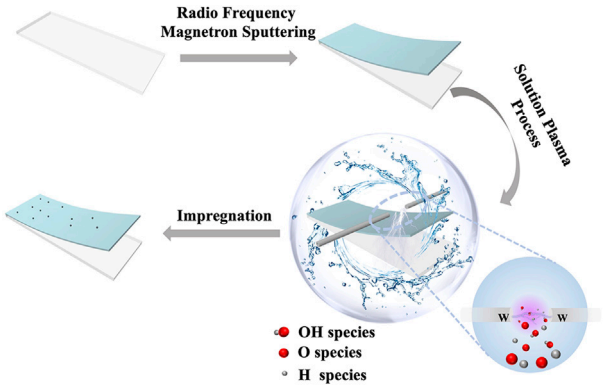

FIGURE 1
Preparation process of MoO_x-Pt-SP electrocatalytic CEs.

immersed in a 0.3 mM N719 ethanol solution and soaked at room temperature for 24 h to complete the dye adsorption and then rinsed three times for 3 s each with ethanol and dried. The DSCs were assembled by sandwiching the sensitized TiO_2 photoanode with an electrocatalytic electrode by introducing an electrolyte containing 0.6 M 1,3-dimethylimidazolium iodide, 0.1 M guanidinium thiocyanate, 0.03 M iodine, 50 mM lithium iodide, and 0.5 M 4-tert-butylprine in acetonitrile/valeronitrile (85:15, v/v).

Solution plasma process

SP was performed as described in detail elsewhere. The sample was placed into a reactor containing 80 ml of deionized water. A tungsten rod and a tungsten tube were used as electrodes. The sample was placed below the inter-electrode gap. Also, the distance between the sample and the two tungsten electrodes was approximately 10 mm. N_2 was introduced into the reactor through the hollow tungsten electrode. Plasma was generated by a bipolar-DC pulsed power supply (Kurita, Japan). The pulse width and frequency were 2.0 μs and 20 kHz, respectively. The temperature of the solution, which was 10°C, was controlled by a water chiller.

Results and discussion

As shown in Figure 1, the MoO_x film (Supplementary Figure S1) was deposited on a clean conductive glass FTO by radio frequency magnetron sputtering (RFMS) and then was treated *via* the SP process. This SP process in the aqueous solution could generate numerous highly reactive species, including H^+, OH^-, and O^{2-} species, due to the ready dissociation of water (Pitchaimuthu et al., 2018). According to the research of our groups, we deem that the H^+ species rapidly diffuses into the plasma/liquid interface bombarding the surface of TiO_2, which causes removal of the oxygen atoms and generates oxygen vacancies since the mass of the H^+ species is less than that of the $OH^-$and O^{2-} species (Yu et al., 2020). Therefore, we consider that MoO_x, which has a similar electronic structure to TiO_2, can also generate oxygen vacancies through the bombardment of H^+ species. Then, the SP-treated MoO_x support was impregnated in the isopropanol solution of chloroplatinic acid for loading the platinum (Pt) nanoclusters. Finally, an electrocatalytic electrode (denoted as MoO_x-Pt-SP) was prepared by thermal annealing in an inert atmosphere (N_2) at 450°C. In contrast, the reference sample (named as MoO_x-Pt) was also prepared by impregnating the MoO_x support without SP treatment into the chloroplatinic acid isopropanol solvent and then annealing at 450°C.

First, we investigated the influence of SP treatment on the oxygen vacancies of MoO_x films by X-ray photoelectron spectroscopy (XPS) and electron spin resonance (ESR). Three peaks of each sample were exhibited clearly in the O1s core-level spectra shown in Figure 2A: the main component peak was deemed as lattice oxygen (Mo-O) located at 530.81 eV; another peak located at 532.44 eV, that is attributed to oxygen in hydroxyl groups (–OH); the last peak at 533.15 eV corresponds to physically adsorbed water (H_2O) (Sendova-Vassileva et al., 2016). The peak area is related to the content of elements. The lattice oxygen peak area of MoO_x is reduced through SP treatment, indicating that SP can generate oxygen vacancies. Figure 2B shows the Mo3d core-level spectra of MoO_x and MoO_x-SP. The Mo3d core-level spectra of MoO_x is composed of two peaks which are attributed to $3d_{3/2}$ and $3d_{5/2}$. Also, $Mo3d_{5/2}$ of MoO_x at 232.75 eV can be assigned to Mo^{6+} species. For the MoO_x-SP sample, $Mo3d_{5/2}$ shifted to a lower binding energy at 232.50 eV, resulting from the electron transfer from the oxygen vacancy to the Mo. Meanwhile, the electron transfer means an increase in electron density and a weaker binding effect of Mo-O (Luo et al., 2016; Li et al., 2021). Moreover, Figure 2C shows that both samples have signals at the oxygen vacancy characteristic spectral line (g = 2.007) by ESR (Ohno, 1986; Poppl and Volkel, 1989; Nakamura et al., 2000). For MoO_x-SP, the intensity of the oxygen vacancy signal increases, manifesting that there are more oxygen vacancies in MoO_x-SP. This is the same as the results of O1s XPS in Figure 2A. All the aforementioned information indicates that SP is an effective approach to introducing oxygen vacancies.

The microstructure of the MoO_x and MoO_x-SP deposited on the silicon wafer is exhibited in Figures 3A,B. Corresponding height profiles in Figure 3C shows that the thickness of the two films is similar, around 3 nm, which indicates that the SP has no impact on the film thickness. To shed light on the role of oxygen vacancies, the electrical conductivity of samples was characterized. We tested the electrochemical impedance spectrum (EIS) of two samples shown in Figure 3D, and the

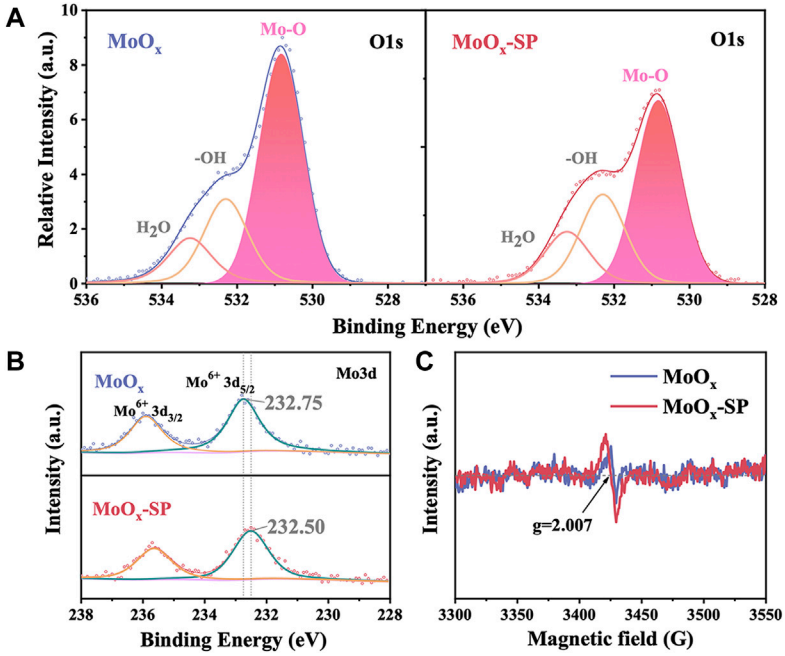

FIGURE 2
O1s **(A)**, Mo3d **(B)** XPS spectra, and ESR spectra **(C)** of MoO_x and MoO_x-SP.

corresponding charge transfer resistance is listed in Table 1. The test structure used is mainly a symmetrical cell structure in the form of CE//electrolyte//CE. EIS results show that the charge transfer resistance (R_{ct}) of MoO_x-SP is lower ($1.20 \times 10^4\ \Omega\ cm^{-2}$) than that of MoO_x ($2.25 \times 10^4\ \Omega\ cm^{-2}$), which may be attributed to the increase of interfacial oxygen vacancy active sites and electrical conductivity owing to the introduction of oxygen vacancies. As shown in Figures 3E,F, conducting atomic force microscopy (C-AFM) demonstrates that the average current of the MoO_x-SP thin film is 0.5300 nA (Table 1), which is two orders of magnitude higher than that of the MoO_x thin film (0.0065 nA) with the same bias voltage. We can discover that the bulk resistance of the MoO_x-SP thin film is lower than that of the MoO_x thin film, considering the nearly identical thickness of the two films. The bulk resistance of MoO_x-SP decreased, suggesting that oxygen vacancies contributed to the improvement of electrical conductivity. We suggest that the oxygen vacancies likely act as shallow donors to increase the carrier concentration, thereby enhancing the electrical conductivity.

According to the previous literature about SMSI, oxygen vacancies were favorable for enhancing the SMSI (Farmer and Campbell, 2010; Jang et al., 2016; Liu et al., 2019) because metal cations in the supports are reduced by the nearby oxygen vacancies, triggering the charge transfer between the reduced metal cation and the catalytic sites. Consequently, we investigated the effect of oxygen vacancies. The Pt4f core-level spectra were deconvoluted into two pairs of doublets in Figure 4A, which can be assigned to Pt^0 and Pt^{2+} species. The more intense doublet is attributed to Pt^0. Comparing the binding energies of $Pt^0 4f_{7/2}$ peak, we could observe that the peak position for MoO_x-Pt-SP (71.30 eV) has a slight shift to higher binding energy in contrast to that of MoO_x-Pt (71.15 eV) treated without the SP. It is proved that MoO_x-Pt-SP with more oxygen vacancies has a reduction in the electron density of platinum sites, which leads to the formation of an electron-rich region between Pt-Mo and substantial changes in the metal–support interaction (Lin et al., 2017). The positive role of oxygen vacancies in SMSI can be verified by Pt4f XPS, which has the potential to enhance the catalytic activity of the electrocatalyst.

In order to characterize the catalytic performance of the samples, EIS was carried out. The test structure used is mainly a symmetrical cell structure in the form of CE//electrolyte//CE. The consequence of EIS can be fitted by Z-View software combined with the equivalent circuit diagram shown in Figure 4B. The equivalent circuit diagram incorporates the series resistance (R_s), which chiefly comprises sheet resistance at the contact point, external wire, and electrode; the interfacial charge transfer resistance (R_{ct}) at the CE/electrolyte interface; the diffusion impedance (Z_w) of the redox couple in the electrolyte; and the interfacial double-layer chemical capacitance (CPE). The EIS is shown in Figure 4B, and its data are summarized in Table 2 after fitting. A slight difference is present in the R_s of MoO_x-Pt and MoO_x-Pt-SP CEs (were 17.02 $\Omega\ cm^{-2}$ and 18.00 $\Omega\ cm^{-2}$, respectively), which may be caused by different contact points

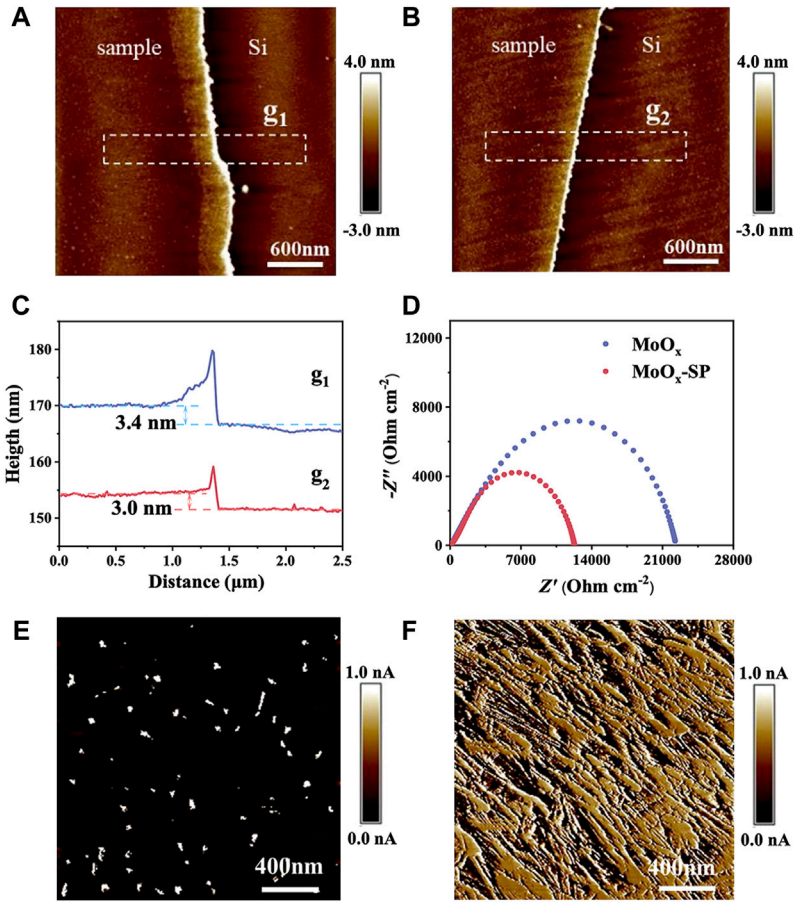

FIGURE 3
AFM surface morphologies of **(A)** the MoO_x and **(B)** MoO_x-SP thin film. The corresponding height profiles **(C)** of the MoO_x and MoO_x-SP thin film in two regions shown in **(A)** (g1) and **(B)** (g2). Nyquist plots **(D)** of the MoO_x and MoO_x-SP thin film. C-AFM images of **(E)** the MoO_x and **(F)** MoO_x-SP thin film.

TABLE 1 Average current and R_{ct} of the MoO_x and MoO_x-SP thin film from C-AFM and EIS results.

Samples	*I* (C-AFM current) (nA)	R_{ct} (EIS) ($\times 10^4\ \Omega\ cm^{-2}$)
MoO_x	0.0065	2.25
MoO_x-SP	0.5300	1.20

and external wire connections during the test. The R_{ct} of MoO_x-Pt-SP CEs is 1.80 $\Omega\ cm^{-2}$, which is 4.20 $\Omega\ cm^{-2}$ lower than that of MoO_x-Pt CEs (R_{ct} = 6.00 $\Omega\ cm^{-2}$). This illustrates that the charge transfer at the interface between the electrocatalytic electrode and electrolyte is easier in MoO_x-Pt-SP.

Apart from the EIS, the Tafel polarization curve test is another main means to characterize the catalytic activity of the electrode, and its test structure is consistent with that of the EIS. Theoretically, the Tafel polarization curve can be divided into three zones: the polarization zone, the Tafel zone, and the diffusion zone. The left branch with negative voltage corresponds to the reduction reaction of I_3^-, which is the focus area, and the right branch with positive voltage corresponds to the oxidation reaction of I^-. The exchange current density (J_0) and the limiting diffusion current density (J_{lim}) can be obtained from the Tafel polarization curve. J_0 is directly related to R_{ct} by the formula: $J_0 = RT/nFR_{ct}$, where R is the gas constant, n (n = 2) is the number of electrons involved in the reduction of I_3^- at the electrode, T is thermodynamic temperature, and F is Faraday constant. Figure 4C shows the polarization curves of the two samples. It is obvious that MoO_x-Pt-SP CEs have higher anode or cathode branches, so their J_0 is larger and they have higher electrocatalytic activity. R_{ct} calculated from J_0 of the Tafel polarization curves is shown in Table 2 and shows that MoO_x-Pt-SP CEs have higher electrocatalytic activity. Consequently, EIS and Tafel polarization curves have the

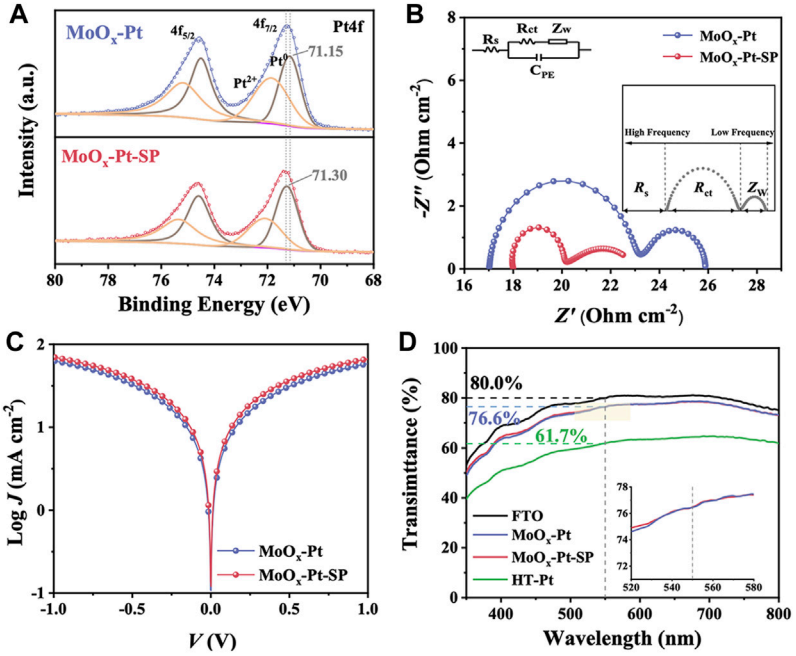

FIGURE 4
Pt4f XPS spectra **(A)** of MoO_x-Pt and MoO_x-Pt-SP. Nyquist plots **(B)** and Tafel polarization curves **(C)** of MoO_x-Pt and MoO_x-Pt-SP electrocatalytic electrodes. Transmittance spectra **(D)** of FTO, MoO_x-Pt, MoO_x-Pt-SP, and HT-Pt electrocatalytic electrodes.

TABLE 2 Summary of R_s and R_{ct} fitted from EIS and Tafel polarization curves of MoO_x-Pt and MoO_x-Pt-SP CEs.

Samples	R_s (Ω cm^{-2})	R_{ct} (EIS) (Ω cm^{-2})	R_{ct} (Tafel) (Ω cm^{-2})
MoO_x-Pt	17.02	6.00	3.21
MoO_x-Pt-SP	18.00	1.80	2.08

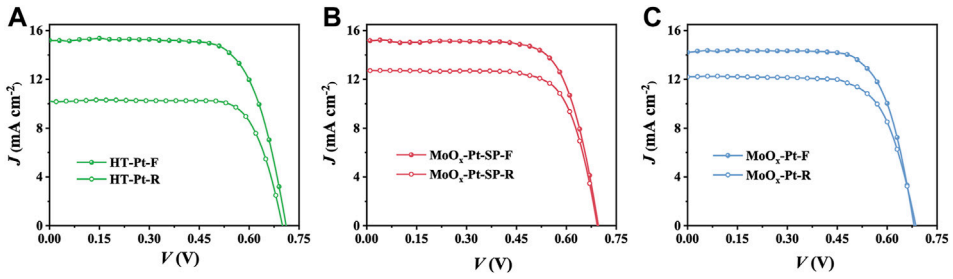

FIGURE 5
J–V curves of DSCs with HT-Pt **(A)**, MoO_x-Pt-SP **(B)**, and MoO_x-Pt **(C)** CEs measured under AM 1.5G 100 mW cm^{-2} from the front (F) and rear (R) sides.

same results, implying that the MoO_x-Pt-SP CEs have higher electrocatalytic activity. The reason may be ascribed to the improvement of the electrocatalytic electrode conductivity caused by the increase of oxygen vacancies. Furthermore, the enhanced SMSI performance caused by oxygen vacancies further dispersed the Pt particles, thereby

TABLE 3 Photovoltaic parameters of DSCs illuminated from the front (F) and rear (R) sides.

CEs	Front (F)				Rear (R)				
	Jsc (mA cm^{-2})	Voc (V)	FF	PCE (%)	Jsc (mA cm^{-2})	Voc (V)	FF	PCE (%)	Retention (%)
HT-Pt	15.20	0.71	0.71	7.65	10.21	0.70	0.76	5.43	71
MoO_x-Pt-SP	15.21	0.70	0.71	7.56	12.71	0.69	0.73	6.41	85
MoO_x-Pt	14.21	0.68	0.72	6.97	12.20	0.68	0.70	5.84	84

increasing the active area of the catalyst. This may be another reason for the better electrocatalytic effect of the MoO_x-Pt-SP electrode.

The optical transmittance of the electrocatalytic electrode impacts the efficiency of the rear side illumination for bifacial DSCs. But Pt CEs (HT-Pt), which were fabricated using the spinning coating method followed by a high-temperature pyrolysis process, have usually been disappointing in transmittance. So, we utilized SMSI to achieve the electrocatalytic electrode with high transmittance. The transmittance of MoO_x-Pt, MoO_x-Pt-SP, HT-Pt CEs, and conductive glass FTO is explored by UV–Vis spectroscopy (Figure 4D). The MoO_x-Pt and MoO_x-Pt-SP CEs show a good optical transmittance of 76.6% at 550 nm, which is only a 3.4% reduction compared to that of the FTO substrate. In contrast, the transmittance of the HT-Pt electrode is 61.7% at 550 nm, which is probably due to light absorption and scattering caused by excessive loading and agglomeration of the Pt (Supplementary Figure S2). The good optical transmittance of MoO_x-Pt and MoO_x-Pt-SP CEs could be ascribed to the good dispersion of the Pt caused by the SMSI character. Although the transmittance of the MoO_x-Pt-SP and MoO_x-Pt CEs is similar in the visible range, the EIS and Tafel polarization curve tests show superior electrocatalytic performance of MoO_x-Pt-SP CEs. Such a transparent electrocatalytic electrode guarantees the realization of bifacial DSCs.

We fabricated DSCs using HT-Pt, MoO_x-Pt-SP, and MoO_x-Pt CEs. Also, the current density–voltage (J–V) curves of DSCs, which were measured under AM 1.5 g 100 mW cm^{-2} from the front (F) and rear (R) sides, are shown in Figure 5. Specific photovoltaic data, including short-circuit current density (J_{sc}), open circuit voltage (V_{oc}), fill factor (FF), and PCE, are summarized in Table 3. The DSCs with MoO_x-Pt CEs produced a PCE of 6.97% under the front illumination. Also, the front-illuminated PCE of the DSCs with MoO_x-Pt-SP CEs is 7.56% (J_{sc} = 15.21 mA cm^{-2}, V_{oc} = 0.70 V, FF = 0.71), which is close to 7.65% for that of conventional Pt CEs. The high catalytic activity of the MoO_x-Pt-SP electrocatalytic electrode was further demonstrated. The rear-illuminated PCE of the MoO_x-Pt-SP cell can reach 6.41% (J_{sc} = 12.71 mA cm^{-2}, V_{oc} = 0.69 V, FF = 0.73), which remains at 85% of the front-side PCE. In comparison, the rear-side efficiency of the Pt cell just retained 71% of the front-illuminated efficiency. The retention rate of the MoO_x-Pt-SP cell is 20% higher than that of the Pt cell. This is attributed to the high transmittance of MoO_x-Pt-SP CEs. So far, we prepared high catalytic activity electrocatalytic electrodes with good transparency.

Conclusions

In conclusion, this work reveals that the SP is an effective method for introducing oxygen vacancies and improving the catalytic performance of SMSI-based MoO_x/Pt CEs for bifacial DSCs. The SP-induced oxygen vacancies enhanced the electrical conductivity of MoO_x support and the interaction between Pt and MoO_x. Consequently, MoO_x/Pt-SP CEs have superior electrocatalytic activity than the untreated reference CEs. The front-illuminated efficiency of the MoO_x-Pt-SP cell (7.56%) is comparable with that of the Pt cell (7.65%). But the rear-illuminated efficiency of the MoO_x-Pt-SP cell reached 6.41%, thus achieving a high rear-to-front efficiency ratio of 85% in contrast with that of 71% for the Pt cell. This suggests the great potential of MoO_x-Pt-SP CEs in high-performance bifacial DSCs. In addition, our work proved the importance of oxygen vacancies in enhancing the activity of TMO-based SMSI electrocatalysts and suggested an efficient SP strategy that could be applied to various electrocatalysis systems.

Data availability statement

The original contributions presented in the study are included in the article/Supplementary Material; further inquiries can be directed to the corresponding authors.

Author contributions

All authors listed have made a substantial, direct, and intellectual contribution to the work and approved it for publication.

Funding

The work was supported by the National Natural Science Foundation of China (62074031 and 51872044), funding from Jilin Province (JJKH20211295KJ), the 111 project (B13013), and the Fundamental Research Funds for the Central Universities (2412019FZ036).

Conflict of interest

The authors declare that the research was conducted in the absence of any commercial or financial relationships that could be construed as a potential conflict of interest.

Publisher's note

Supplementary material

The Supplementary Material for this article can be found online at: https://www.frontiersin.org/articles/10.3389/fenrg.2022.924515/full#supplementary-material

References

Chen, M., Shao, L., Lv, X., Wang, G. C., Yang, W. Q., Yuan, Z. Y., et al. (2020). *In situ* growth of Ni-encapsulated and N-doped carbon nanotubes on N-doped ordered mesoporous carbon for high-efficiency triiodide reduction in dye-sensitized solar cells. *Chem. Eng. J.* 390, 124633. doi:10.1016/j.cej.2020.124633

Duan, Y., Tang, Q., He, B., Li, R., and Yu, L. (2014). Transparent nickel selenide alloy counter electrodes for bifacial dye-sensitized solar cells exceeding 10% efficiency. *Nanoscale* 6, 12601–12608. doi:10.1039/c4nr03900a

Farmer, J., and Campbell, C. (2010). Ceria maintains smaller metal catalyst particles by strong metal-support bonding. *Science* 329, 933–936. doi:10.1126/science.1191778

Ge, Y., Qin, X., Li, A., Deng, Y., Lin, L., Zhang, M., et al. (2021). Maximizing the synergistic effect of CoNi catalyst on alpha-MoC for robust hydrogen production. *J. Am. Chem. Soc.* 143, 628–633. doi:10.1021/jacs.0c11285

Guo, Y., Mei, S., Yuan, K., Wang, D. J., Liu, H. C., Yan, C. H., et al. (2018). Low-temperature CO_2 methanation over CeO_2-supported Ru single atoms, nanoclusters, and nanoparticles competitively tuned by strong metal–support interactions and H-spillover effect. *ACS Catal.* 8, 6203–6215. doi:10.1021/acscatal.7b04469

Han, B., Guo, Y., Huang, Y., Xi, W., Xu, J., Luo, J., et al. (2020). Strong metal-support interactions between Pt single atoms and TiO_2. *Angew. Chem. Int. Ed.* 59, 11824–11829. doi:10.1002/anie.202003208

Ito, S., Zakeeruddin, S., Comte, P., Liska, P., Kuang, D., and Gratzel, M. (2008). Bifacial dye-sensitized solar cells based on an ionic liquid electrolyte. *Nat. Photonics* 2, 693–698. doi:10.1038/nphoton.2008.224

Jang, M., Agarwal, R., Nukala, P., Choi, D., Johnson, A. T. C., Chen, I. W., et al. (2016). Observing oxygen vacancy driven electroforming in Pt-TiO_2-Pt device via strong metal support interaction. *Nano Lett.* 16, 2139–2144. doi:10.1021/acs.nanolett.5b02951

Jedsukontorn, T., Ueno, T., Saito, N., and Hunsom, M. (2018). Narrowing band gap energy of defective black TiO_2 fabricated by solution plasma process and its photocatalytic activity on glycerol transformation. *J. Alloys Compd.* 757, 188–199. doi:10.1016/j.jallcom.2018.05.046

Li, H., Wang, Z., Jing, H., Yi, S. S., Zhang, S. X., Yue, X. Z., et al. (2021). Synergetic integration of passivation layer and oxygen vacancy on hematite nanoarrays for boosted photoelectrochemical water oxidation. *Appl. Catal. B Environ.* 284, 119760. doi:10.1016/j.apcatb.2020.119760

Li, Q., Zhu, X., Yang, J., Yu, Q., Zhu, X., Chu, J., et al. (2020). Plasma treated Bi_2WO_6 ultrathin nanosheets with oxygen vacancies for improved photocatalytic CO_2 reduction. *Inorg. Chem. Front.* 7, 597–602. doi:10.1039/c9qi01370a

Lin, L., Zhou, W., Gao, R., Yao, S., Zhang, X., Xu, W., et al. (2017). Low-temperature hydrogen production from water and methanol using Pt/α-MoC catalysts. *Nature* 544, 80–83. doi:10.1038/nature21672

Liu, G., Li, J., Fu, J., Jiang, G., Lui, G., Luo, D., et al. (2019). An oxygen-vacancy-rich semiconductor-supported bifunctional catalyst for efficient and stable zinc-air batteries. *Adv. Mat.*, 31. e1806761. doi:10.1002/adma.201806761

Luo, Z., Miao, R., Huan, T., Mosa, I. M., Poyraz, A. S., Zhong, W., et al. (2016). Mesoporous MoO_{3-x} material as an efficient electrocatalyst for hydrogen evolution reactions. *Adv. Energy Mat.* 6, 1614–6832. doi:10.1002/aenm.201600528

Nakamura, I., Negishi, N., Kutsuna, S., Ihara, T., Sugihara, S., and Takeuchi, K. (2000). Role of oxygen vacancy in the plasma-treated TiO_2 photocatalyst with visible light activity for NO removal. *J. Mol. Catal. A Chem.* 161, 205–212. doi:10.1016/s1381-1169(00)00362-9

Ohno, K. (1986). ESR imaging and its applications. *Appl. Spectrosc. Rev.* 22, 1–56. doi:10.1080/05704928608060437

Pitchaimuthu, S., Honda, K., Suzuki, S., Naito, A., Suzuki, N., Katsumata, K. i., et al. (2018). Solution plasma process-derived defect-induced heterophase Anatase/brookite TiO_2 nanocrystals for enhanced gaseous photocatalytic performance. *ACS Omega* 3, 898–905. doi:10.1021/acsomega.7b01698

Poppl, A., and Volkel, G. (1989). ESR investigation of the oxygen vacancy in pure and Bi_2O_3-doped zno ceramics. *Phys. Stat. Sol. (a)* 115, 247–255. doi:10.1002/pssa.2211150127

Sendova-Vassileva, M., Dikov, H., Vitanov, P., Popkirov, G., Gergova, R., Grancharov, G., et al. (2016). Magnetron sputtered molybdenum oxide for application in polymers solar cells. *J. Phys. Conf. Ser.* 764, 012022. doi:10.1088/1742-6596/764/1/012022

Takai, O. (2014). Fundamentals and applications of solution plasma. *J. Photopol. Sci. Technol.* 27, 379–384. doi:10.2494/photopolymer.27.379

Tauster, S., and Fung, S. (1978). Strong metal-support interactions Occurrence among the binary oxides of groups IIA–VB. *Chem. Eng. J.* 55, 29–35. doi:10.1016/0021-9517(78)90182-3

Tauster, S. (1987). Strong metal-support interactions. *Acc. Chem. Res.* 20, 389–394. doi:10.1021/ar00143a001

Tian, Y., Wang, Y., Chen, S., Gu, Z. G., and Zhang, J. (2020). Epitaxial growth of highly transparent metal-porphyrin framework thin films for efficient bifacial dye-sensitized solar cells. *ACS Appl. Mat. Interfaces* 12, 1078–1083. doi:10.1021/acsami.9b19022

Tran, S., Choi, H., Oh, S., and Park, J. Y. (2019). Defective Nb_2O_5-supported Pt catalysts for CO oxidation: Promoting catalytic activity via oxygen vacancy engineering. *J. Catal.* 375, 124–134. doi:10.1016/j.jcat.2019.05.017

Wang, C., Li, Y., Zhang, C., Chen, X., Liu, C., Weng, W., et al. (2021). A simple strategy to improve Pd dispersion and enhance Pd/TiO_2 catalytic activity for formaldehyde oxidation: The roles of surface defects. *Appl. Catal. B Environ.*, 282, 119540. doi:10.1016/j.apcatb.2020.119540

Wang, G., Li, Y., and Ling, Y. (2012). Oxygen-deficient metal oxide nanostructures for photoelectrochemical water oxidation and other applications. *Nanoscale* 4, 6682–6691. doi:10.1039/c2nr32222f

Wang, S., He, T., Chen, P., Du, A., Ostrikov, K., Huang, W., et al. (2020). *In situ* formation of oxygen vacancies achieving near-complete charge separation in planar $BiVO_4$ photoanodes. *Adv. Mat.*, 32. 202001385, doi:10.1002/adma.202001385

Wu, C., Li, R., Wang, Y., Lu, S., Lin, J., Liu, Y., et al. (2020). Strong metal-support interactions enable highly transparent Pt-Mo_2C counter electrodes of bifacial dye-sensitized solar cells. *Chem. Commun.* 56, 10046–10049. doi:10.1039/d0cc03744c

Xu, T., Kong, D., Tang, H., Qin, X., Li, X., Gurung, A., et al. (2020). Transparent MoS_2/PEDOT composite counter electrodes for bifacial dye-sensitized solar cells. *ACS Omega* 5, 8687–8696. doi:10.1021/acsomega.0c00175

Yan, D., Wang, W., Luo, X., Chen, C., Zeng, Y., and Zhu, Z. (2018). $NiCo_2O_4$ with oxygen vacancies as better performance electrode material for supercapacitor. *Chem. Eng. J.* 334, 864–872. doi:10.1016/j.cej.2017.10.128

Yu, F., Wang, C., Li, Y., Ma, H., Wang, R., Liu, Y., et al. (2020). Enhanced solar photothermal catalysis over solution plasma activated TiO_2. *Adv. Sci. (Weinh).* 7, 2000204. doi:10.1002/advs.202070092

Yu, J., Sun, X., Tong, X., Zhang, J., Li, J., Li, S., et al. (2021). Ultra-high thermal stability of sputtering reconstructed Cu-based catalysts. *Nat. Commun.* 12, 7209. doi:10.1038/s41467-021-27557-1

Yu, Y., Jin, R., Easa, J., Lu, W., Yang, M., Liu, X., et al. (2019). Highly active and stable copper catalysts derived from copper silicate double-shell nanofibers with strong metal-support interactions for the RWGS reaction. *Chem. Commun.* 55, 4178–4181. doi:10.1039/c9cc00297a

Zhang, J., Wang, H., Wang, L., Ali, S., Wang, C., Wang, L., et al. (2019). Wet-chemistry strong metal-support interactions in titania-supported Au catalysts. *J. Am. Chem. Soc.* 141, 2975–2983. doi:10.1021/jacs.8b10864

Zheng, T., Sang, W., He, Z., Wei, Q., Chen, B., Li, H., et al. (2017). Conductive tungsten oxide nanosheets for highly efficient hydrogen evolution. *Nano Lett.* 17, 7968–7973. doi:10.1021/acs.nanolett.7b04430